

# 40-Gb/s Widely Tunable Transceivers

James W. Raring and Larry A. Coldren

(Invited Paper)

**Abstract**—We present the first monolithic widely tunable 40-Gb/s transceivers. The devices integrate sampled grating distributed Bragg reflector (SG-DBR) lasers, quantum-well electroabsorption modulators (EAM), low-confinement semiconductor optical amplifiers (SOA), and uni-traveling carrier (UTC) photodiodes for state-of-the-art light generation, modulation, amplification, and detection. A relatively simple high-flexibility fabrication scheme combining quantum-well intermixing (QWI) and blanket metal-organic chemical vapor deposition (MOCVD) regrowth was used to integrate components with performance rivaling optimized discrete devices. The SG-DBR/EAM transmitters demonstrate 30 nm of tuning, 39-GHz bandwidth, low-drive voltage, and low power penalty 40-Gb/s transmission through 2.3 km of fiber. The SOA/UTC photodetector receivers provide 23–28 dB of gain, saturation powers up to 18.6 dBm, and –20.2 dBm of chip-coupled sensitivity at 40 Gb/s. By connecting the transmitters and receivers off-chip, we demonstrate 40-Gb/s wavelength conversion.

**Index Terms**—Electroabsorption modulators, photodetectors, semiconductor lasers, semiconductor optical amplifiers, transceivers, wavelength converters.

## I. INTRODUCTION AND MOTIVATION

THE monolithic integration of highly optimized photonic devices onto a single chip could revolutionize lightwave communications as it is perhaps the only way to truly revitalize the optical component industry. The generation, detection, modulation, amplification, switching, and transport of light on a single chip allows for a new generation of high-functionality photonic integrated circuits (PICs) with reduced cost, size, and power dissipation. Since fiber is not required for light transfer between components, PICs do not suffer from the device-to-device coupling problem of systems comprised of discrete components. The removal of the coupling loss allows for a reduction in power dissipation because lower drive currents will be required to achieve equivalent power levels to and from the device. Fewer packages are necessary since multiple components can be housed within a single enclosure. Device reliability is improved from the elimination of possible mechanical movements among the optical elements and from the reduced drive current requirements.

The potential benefits of monolithic integration fueled the pioneering efforts of the late 1980s and early 1990s to develop increased functionality chips [1]. During this time, researchers

made great advances with the demonstration of distributed feedback (DFB) laser/modulators, highly functional balanced heterodyne receivers, and integrated mode converters [2]–[4]. Despite this early progress, the PIC has failed to scale at the same Moore's Law rate of the integrated circuit (IC) [5]. This can be largely attributed to the difficulty associated with optimizing the diverse components required in high-functionality photonic chips. Ever-increasing bit rate demands amplify this challenge since the individual components will necessitate more exotic structures for efficient, high-speed operation.

Low-threshold current, high-output power diode lasers benefit from maximized modal gain within the active section. By placing quantum wells (QWs) in the center of a symmetric waveguide, the optical confinement factor and hence the modal gain can be maximized within the laser [6]. The electroabsorption modulator (EAM) is an attractive modulator due to its compact size, simple fabrication, high modulation bandwidth, and high efficiency. To achieve negative chirp along with high modulation efficiency from relatively short devices for 40-Gb/s operation, QW absorber regions are required to exploit the quantum confined Stark effect (QCSE) [7]. Low optical confinement QW active regions are a popular choice for use in semiconductor optical amplifiers (SOAs) requiring high-saturation powers since the photon density within the QWs can be kept relatively low. Using this scheme, impressive saturation powers of +23 dBm have been demonstrated [8]. The uni-traveling carrier (UTC) photodiode has been developed specifically to eliminate the influence of hole transport on the operation of the photodetector such that the classic space charge effect plaguing the performance of conventional p-i-n detectors can be avoided. Since the carrier transport properties are dominated by electrons, saturation current densities, 4–6 times higher than that in p-i-n photodiodes, are theoretically possible, enabling high-power, high-speed operation [9].

Defining these unique components on a single chip to realize a high-performance transceiver is a demanding task due to the common two-dimensional (2-D) growth and processing platforms used for device fabrication. Simple integration schemes limit design flexibility, imposing a performance penalty within the PIC. Complex schemes with increased flexibility can lead to decreased yield, driving the device cost upwards. For the potential benefits of PICs to win out over discrete devices, the integration must be accomplished in a manner as to provide high device yield and repeatability at low cost.

## II. BACKGROUND: METHODS OF MONOLITHIC INTEGRATION

In Fig. 1, we present several integration platforms used for high-functionality PIC fabrication. The butt-joint regrowth

Manuscript received June 22, 2006; revised September 13, 2006. This work was supported in part by Defense Advanced Research Projects Agency/Microsystems Technology Office (DARPA/MTO) CS-WDM under Grant N66001-02-C-8026 and in part by Intel Corporation under Grant TXA001630000.

The authors are with the Department of Electrical Engineering, University of California, Santa Barbara, CA 93106 USA (e-mail: jraring@engineering.ucsb.edu).

Digital Object Identifier 10.1109/JSTQE.2006.885329

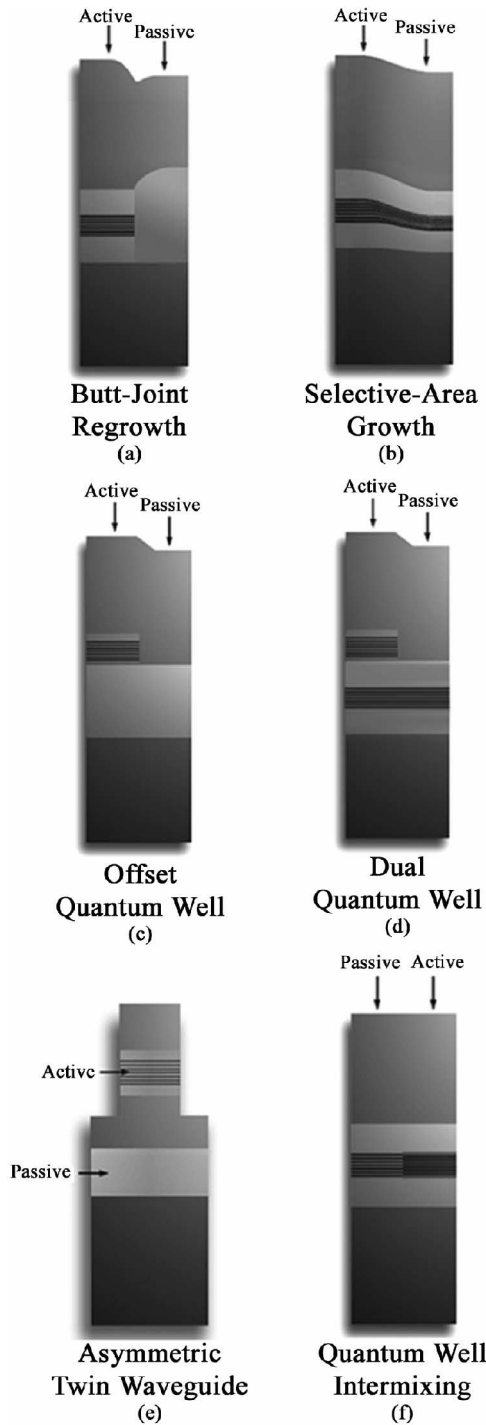


Fig. 1. Various techniques for achieving active and passive sections orthogonal to the growth direction.

(BJR) method in Fig. 1(a) offers a high degree of versatility. This method involves the selective removal of the base structure, as-grown multiple-quantum-well (MQW) active region followed by the nonplanar selective regrowth of an alternative material structure with the desired band-edge in the core of the waveguide. The BJR process enables the use of a centered MQW (c-MQW) active region for maximized modal gain in the laser, and allows each integrated component to possess a unique band-edge

and/or epitaxial structure. The drawback to this method is the difficulty associated with achieving high-quality butt-joint interfaces across the chip to avoid reflections and losses in the core of the optical waveguide [10], [11]. Furthermore, this method relies on a dielectric mask to prevent deposition in specified areas during growth. As the PIC functionality is increased to the transceiver level where more active architectures are required, the complexity of BJR process is compounded with additional BJR steps.

Selective area growth (SAG), as shown in Fig. 1(b), has proven to be useful in providing multiple band-edges across a single wafer in one growth step [12]. In this method a dielectric mask is patterned on the wafer, which is then subjected to metal-organic chemical vapor deposition (MOCVD) growth. Growth is limited to regions between the dielectric mask, where the thickness and the composition of the growing layers are modified based on the mask pattern. This technique allows for the definition of c-MQW active regions on the same chip as blue-shifted MQW regions for use in EAMs and passive sections. Beyond this, SAG does not afford much flexibility since the epitaxial architecture is fixed in all components. The SOA and photodetector are forced to employ the same high-confinement MQW structure as used in the laser, resulting in low-saturation power in both receiver components. Since SAG exploits the contrast in surface kinetics of the growth constituents on the semiconductor and dielectric, a high degree of calibration/optimization must be performed to tightly control the MOCVD reactor conditions.

An established and simple integration platform is based on the use of offset QWs, where the MQW active region is grown above a passive bulk waveguide. The MQW is selectively etched in regions where gain is not required, leaving the nonabsorbing waveguide as shown in Fig. 1(c). Although this process only requires a single, blanket-type regrowth, it allows for only two band-edges on a single-chip. The modal gain in the offset QW design is less than optimal since the peak of the optical mode is offset from the MQW. This scheme forces the use of bulk Franz-Keldysh (FK) type EAMs, which are not as efficient as QW-EAMs utilizing the QCSE [7], [13].

In the dual QW platform, as shown in Fig. 1(d), an MQW is grown in the center of the bulk waveguide below the offset MQW, such that a second QW band-edge is defined on the single-chip [14]. The dual QW platform does not provide optimal modal gain to the laser active region since the peak of the mode is offset from the wells. Additionally, this scheme imposes a passive loss versus EAM efficiency tradeoff. The EAM efficiency will increase as the waveguide MQW bandgap energy is decreased, however, this will also increase the passive loss since the waveguide wells are present throughout the device. To manage this tradeoff, longer EAM lengths are used at the expense of bandwidth [14]. In the dual QW and offset QW platforms, SOAs are forced to employ the same MQW structure as the laser, and the photodetector must use either the MQW or the waveguide material as the absorber [15]. The relatively high confinement factor in the active MQW will result in low-SOA saturation power. The high-confinement factor p-i-n structure is not an optimal architecture for high-power, high-speed photodiodes [9].

In the asymmetric twin waveguide (ATG) integration scheme shown in Fig. 1(e), multiple waveguides are grown on top of each other with a transparent InP layer separating them. Active/passive integration is realized by selective removal of the upper “active” waveguide such that only the lower “passive” waveguide remains in regions where active functions are not required. The optical power is coupled between the even and odd modes supported by the waveguide using carefully designed taper couplers [16]. This technique eliminates the need for regrowth only in applications where vertical current injection is not required in grating regions for high-efficiency tuning, which are not applicable to wavelength-agile PICs. Although this platform can enable multiple functions on a single chip, the nature of the vertical coupling into different epitaxial layers would create great difficulty when defining additional active component architectures beyond the two found in the laser/modulator transmitters or the SOA/photodetector receivers devices reported in [17]. That is, the ATG platform does not appear fit for the simultaneous integration of high-confinement MQW active regions for high-gain, low-confinement MQW active regions for high-saturation power, a high-confinement blue-shifted MQW for high-efficiency EAMs, and high-saturation current photodetector structures such as the UTC.

Quantum-well intermixing (QWI), as shown in Fig. 1(f), allows for the strategic, post-growth tuning of multiple QW band-edges without introducing difficult growth steps or discontinuities in the axial waveguide. QWI has been used in the past to fabricate a multitude of devices and there are a number of techniques that have evolved over the years to accomplish selective intermixing, such as impurity-induced disordering (IID) [18], impurity-free vacancy-enhanced disordering (IFVD) [19], photoabsorption-induced disordering (PAID) [20], and implantation-enhanced interdiffusion [21].

QWI enables the use of a c-MQW active region for maximized modal gain in lasers and blue-shifted QWs in the EAMs, and thus breaks the tradeoff of the simplicity offered by the offset QW method and the flexibility offered by BJR and SAG. Since multiple QW band-edges can be defined on a single chip, the passive and EAM band-edges can be independently optimized to avoid the passive loss versus EAM efficiency tradeoff of the dual QW platform. QWI does not change the average composition of the MQW such that there is a negligible index discontinuity at the interface between adjacent sections. This eliminates parasitic reflections that can degrade performance.

### III. NOVEL HIGH-FLEXIBILITY INTEGRATION PLATFORM

Here, we employ a high-flexibility integration method combining an impurity-free implant-enhanced QWI technique with simple blanket MOCVD regrowth. The QWI process uses a single implant to introduce point defects in an undoped InP buffer layer grown above the QWs [22], [23]. Thermal propagation steps are used to diffuse the point defects through the MQW to shift the band-edge. Selective removal of the buffer layer is used to halt the intermixing process in regions where the desired band-edge has been achieved. This process allows for the realization of any number of band-edges on a single-chip, as

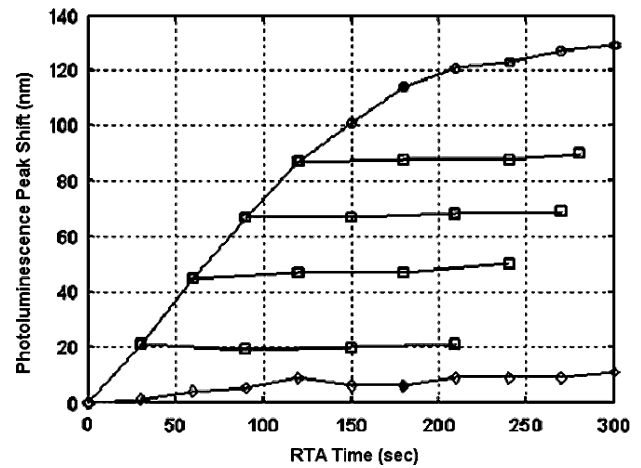


Fig. 2. Peak PL peak shift as a function of anneal time, showing the initial linear increase in the peak shift and the complete halting of the peak shift for samples for which the implant buffer layer has been etched. Symbols indicate nonimplanted (diamonds), implanted (circles), and samples with partial anneal followed by the removal of the implant buffer layer (squares).

the number is determined only by the number of times the thermal processing is interrupted such that the buffer layer can be selectively removed in specified regions. In Fig. 2, the characteristic band-edge shift versus anneal time is shown for implanted regions with and without the buffer layer and for regions not subjected to the implant. A thorough description of the QWI process along with an overview of the PICs fabricated using this technique can be found in [23].

Although QWI provides a simple method to achieve multiple QW band-edges on a single chip for high-performance lasers and QW-EAMs, alone it does not provide the capability to integrate optimal architectures for high-saturation power SOAs and specialized photodetectors. By combining blanket MOCVD regrowth steps with the multiple band-edge QWI process, we present a method to define state-of-the-art lasers, modulators, SOAs, and photodetectors on a single chip without BJR or SAG. The PIC designer is not only free to control the MQW band-edge in the growth plane, but now has the flexibility to control the MQW band-edge in the direction normal to the growth plane and to define unique architectures in the SOAs and photodetectors.

First, QWI is used to define three unique QW bandgaps in the high-confinement base structure c-MQW for use in the laser, EAM, and passive sections. Next, simple blanket MOCVD regrowth and wet etch steps are carried out to define a low-confinement offset MQW (o-MQW) for use in SOAs and UTC photodiode structures. A side-view schematic of a single-chip possessing the four state-of-the-art architectures is shown in Fig. 3.

The key attribute of this high-flexibility scheme is that it requires only simple blanket regrowth steps for the added functionality. The platform does not require the disruption of the waveguide core with regrowth interfaces as does the butt-joint method. The slight discontinuities created in this scheme reside above the intermixed c-MQW waveguide core such that only the tail of the propagating mode encounters them. Furthermore, our process requires no complicating dielectric patterns to remain on

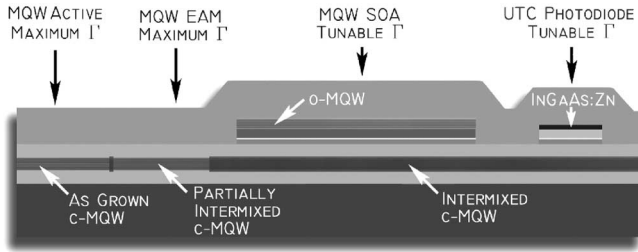


Fig. 3. Schematic side-view of various component architectures that can be defined on a single chip using the QWI and MOCVD regrowth high-flexibility integration scheme.

the semiconductor surface to prevent deposition during growth as in the BJR or SAG methods.

Using the high-flexibility integration scheme, we demonstrate single-chip widely tunable 40-Gb/s transceivers. The widely tunable transmitters demonstrate over 30 nm of tuning with 3-dB optical bandwidths up to 39 GHz and low-drive voltages at 40 Gb/s. The power penalty for 40-Gb/s transmission through 2.3 km of fiber was less than 0.5 dB across the device tuning range. These transmitters represent the first widely tunable EAM-based 40-Gb/s devices and achieve performance levels rivaling state-of-the-art single frequency transmitters requiring BJR [24]. The receiver SOAs provide 23–28 dB of gain with saturation powers in the 18.5-dBm range while the UTC photodiodes exhibit 40-Gb/s operation under high photocurrent conditions. The 40-Gb/s chip-coupled sensitivity of better than  $-20$  dBm is competitive with discrete SOA/photodiode receivers requiring BJR [25]. By connecting the receiver and the transmitter off-chip, we demonstrate low power-penalty widely tunable 40-Gb/s wavelength conversion.

#### IV. 40-Gb/s TRANSCEIVER ARCHITECTURE

The 40-Gb/s transceiver devices employed a parallel surface ridge waveguide architecture with one ridge functioning as the transmitter and the adjacent ridge functioning as the receiver. The  $3\text{-}\mu\text{m}$ -wide surface ridge transmitter consisted of a five-section widely tunable sampled grating distributed Bragg reflector (SG-DBR) laser as described in [26] and a QW-EAM with a length of 125 or 175  $\mu\text{m}$ . Select transmitters made use of a high-gain c-MQW output SOA positioned before the EAM or a high-saturation power o-MQW output SOA positioned after the EAM. Two different receiver designs were explored, both consisted of a  $5\text{-}\mu\text{m}$ -wide dual section SOA and a 3 by 30  $\mu\text{m}$  or 3 by 40- $\mu\text{m}$  UTC photodiode. The SOAs contained a short high-gain c-MQW front-end followed by a long high-saturation power o-MQW section. Curved and flared input/output waveguides were used to reduce the demands on the antireflection coating. A labeled top-view scanning electron micrograph (SEM) image of a transceiver containing the high-saturation power output SOA with a footprint of 0.5 by 3.5 mm is shown in Fig. 4.

#### V. 40-Gb/s TRANSCEIVER FABRICATION SEQUENCE

Device fabrication begins with the MOCVD growth of a c-MQW base structure (Fig. 5) on a sulfur doped InP substrate.

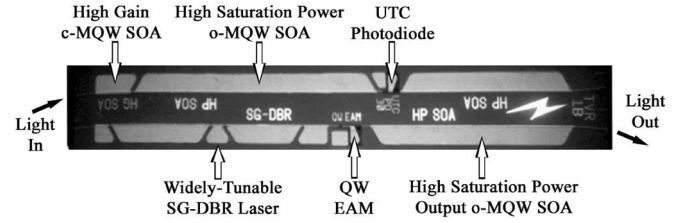


Fig. 4. Top-view SEM image of single-chip 40-Gb/s transceiver with a 0.5 by 3.5 mm footprint.

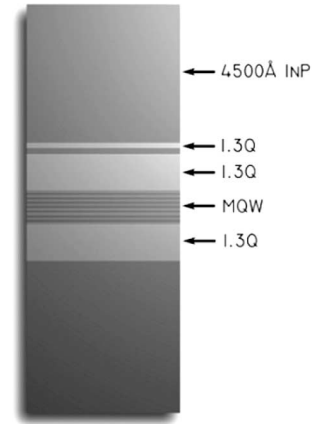


Fig. 5. Epitaxial base structure employing c-MQW active region.

The base structure consists of ten 6.5-nm quantum wells and eight 8.0-nm barriers sandwiched between two 105-nm-thick 1.3Q waveguide layers designed for a maximized optical confinement of 12.6%. The as-grown c-MQW had a peak photoluminescence (PL) emission wavelength of 1540 nm. A 25-nm InP regrowth layer, a 20-nm 1.3Q stop etch layer, and a 450-nm InP layer were grown above the upper waveguide. The top most InP layer, called the implant buffer layer, was designed to capture a low-energy ion implant.

A complete step-by-step schematic illustrating the high-flexibility integration scheme is presented in Fig. 6. After growth of the base structure, a 500-nm  $\text{Si}_x\text{N}_y$  mask layer is deposited using plasma enhanced chemical vapor deposition and lithographically patterned such that it remains only in regions where high-gain c-MQW active regions are desired on the chip. In step 2, an ion implantation is performed using  $\text{P}^+$  at an energy of 100 keV, with a dose of  $5 \times 10^{14} \text{ cm}^{-2}$ , and a substrate temperature of  $200^\circ\text{C}$  to yield a damage range of 90 nm [22]. The point defects created during the  $\text{P}^+$  implant are then partially diffused through the c-MQW structure during a  $\sim 30\text{-s}$  rapid thermal anneal (RTA) at  $675^\circ\text{C}$ , yielding the desired peak PL wavelength of 1505 nm in the EAM sections. The point defects promote the interdiffusion of the well/barrier constituents, reshaping the MQW profile by distorting the well/barrier interface. The result is a shift in the quantized energy levels in the well, and hence a shift in the band-edge energy.

In step 4, the implant buffer layer above the EAM sections is removed using a wet etching process, terminating on the 1.3Q stop etch layer. The sample is then subjected to an additional  $\sim 180\text{-s}$  RTA step to further blue-shift the regions where the implant buffer layer remains. In step 5, the remaining buffer

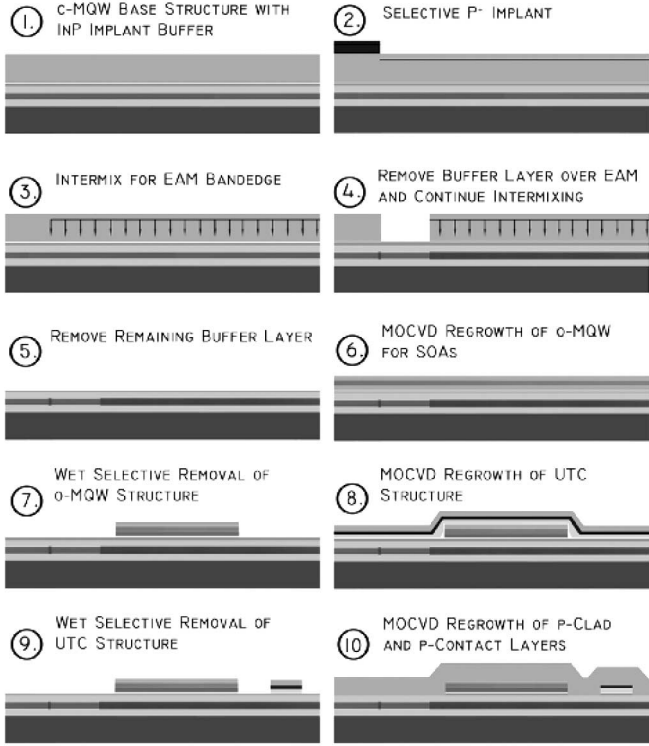


Fig. 6. Step-by-step illustration of high-flexibility integration scheme.

layer and the 1.3Q stop etch layers are removed using wet etching.

A blanket MOCVD regrowth is performed in step 6 for the growth of a thin InP:Si layer, followed by a 1.3Q:Si stop etch layer, an InP:Si confinement tuning layer (CTL), a low-confinement o-MQW active region with similar compositions and thicknesses to that of the base structure c-MQW design, 50 nm of InP, and a 200-nm InP:Zn cap layer. The CTL layer functions to offset the active wells from the peak of the optical mode influencing the confinement factor. Therefore, the choice of the CTL thickness is a key aspect in the SOA design. In this paper, we use five offset wells and choose the CTL thickness to yield a confinement factor of  $\sim 1.4\%$ . Further details of the regrowth aspects and the influence of the CTL thickness can be found in [27].

Following the regrowth, the sample is patterned with  $\text{Si}_x\text{N}_y$  and a wet chemical selective etch sequence is carried out such that the o-MQW structures remain in regions where low confinement SOAs are desired, as shown in step 7. In step 8, a second blanket MOCVD regrowth is performed for the definition of the UTC photodiode structure. Again, the regrowth initiates with a thin InP:Si regrowth layer and a 1.3Q:Si stop etch layer, but is then followed by the growth of a thin InP:Si layer, a 200-nm unintentionally doped InP collector layer, conduction band smoothing layers based on those given in [9], a 50-nm InGaAs:Zn absorber layer, and a 150-nm InP:Zn cap layer. The thickness and doping of both the collector and absorber layers have a great impact on the expected device performance. Further details of the offset UTC structure can be found in [28]. The sample is patterned with  $\text{Si}_x\text{N}_y$  and a

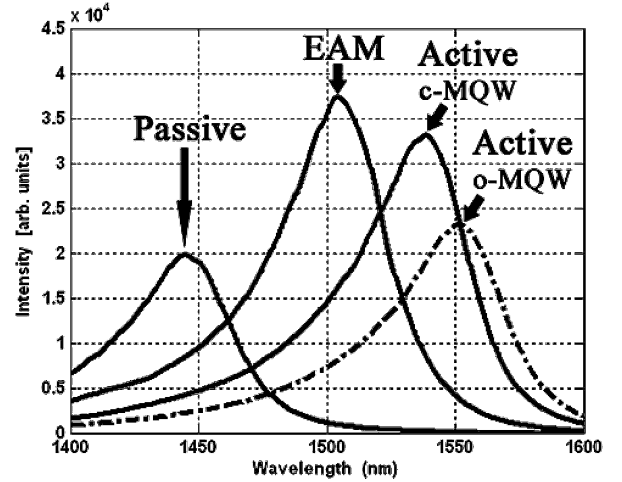


Fig. 7. PL spectra of c-MQW active, EAM, and passive sections along with the regrown o-MQW gain region (dashed).

wet etch is performed to define the UTC structure only where detectors are desired as shown in step 9.

In step 10, a final blanket MOCVD regrowth is performed to grow the p-type InP:Zn cladding and p-contact InGaAs:Zn layers such that four distinct regions remain on a single chip: the as-grown c-MQW active regions to be used for high-gain lasers and SOA sections, the partially intermixed c-MQW regions for use in high-efficiency QW-EAMs, low-confinement o-MQW regions grown above intermixed wells for high-saturation power SOAs, and finally UTC structures grown over intermixed wells for high-saturation power high-bandwidth photodiodes. The PL spectra from the four unique QW band-edges on the single-chip are shown in Fig. 7.

Following the growth sequence, standard lithography and etch techniques were carried out for the definition surface ridge devices. The wafers were thinned, the devices were cleaved into bars and anti-reflection coated. The die were separated, soldered to aluminum nitride carriers, and wire bonded for characterization.

## VI. DEVICE RESULTS

### A. Material Efficiency and Loss Characterization

It is good practice to test diagnostic structures to determine the basic quality of the epitaxial material before examining the high-level PICs. The cleave-back method was used to measure the differential efficiency versus length of 3- $\mu\text{m}$ -wide c-MQW and 5- $\mu\text{m}$ -wide o-MQW surface ridge Fabry–Perot (FP) active lasers identical to the gain region of the lasers and SOAs. With this data, the injection efficiency and modal loss within the gain regions of the PICs was extracted.

A plot of inverse differential efficiency versus FP laser length is presented in Fig. 8 for both the c-MQW and o-MQW devices. The injection efficiency was extracted to be 76% and 74% and the modal loss was extracted to be 18.9 and 3.0  $\text{cm}^{-1}$  in the c-MQW and o-MQW gain regions, respectively. The low modal loss in the o-MQW gain region is essential for high-performance SOA operation since the low optical confinement will result in low incremental modal gain. Therefore, small

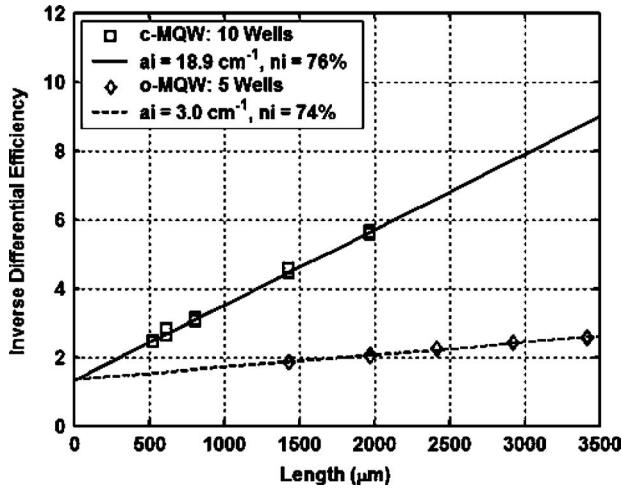


Fig. 8. Plot of inverse differential efficiency versus active FP laser length for lasers fabricated from c-MQW and o-MQW gain sections.

changes in the propagation losses will greatly influence the large signal gain. Future work could focus on reducing this loss value for improved performance.

It is important that the propagation loss in the passive waveguide, mirror, phase, and EAM sections of the device are kept low such that high output powers can be achieved. To study this characteristic we fabricated active/passive FP lasers, where the passive regions are composed of an intermixed MQW. The propagation loss in the passive and EAM sections was extracted at a wavelength of 1550 nm by successively cleaving back the passive/EAM portions of the active/passive lasers and then measuring the differential efficiency when subjecting the active region to pulsed current injection. By constructing a plot of the differential efficiency versus passive/EAM region length, theoretical curves can be fit to the experimental data to extract the loss as described in [6].

Fig. 9 plots the experimental differential efficiency versus passive region length along with theoretical fits for the passive and EAM c-MQW regions on the chip. The passive loss was extracted to be  $1.8 \text{ cm}^{-1}$  and the EAM loss was found to be  $13 \text{ cm}^{-1}$  at a wavelength of 1550 nm. This corresponds to a passive propagation loss of 1 dB/mm and an unbiased insertion loss of  $\sim 1 \text{ dB}$  for a 175- $\mu\text{m}$ -long EAM.

#### B. 40-Gb/s SG-DBR/EAM Transmitter Performance

The continuous wave performance of the transmitters was characterized at a stage temperature of  $18^\circ\text{C}$ . The surface ridge SG-DBR lasers demonstrated over 30 nm of continuous tuning from wavelengths of 1536–1569 nm. In Fig. 10, we present superimposed output spectrums for lasing wavelengths across the SG-DBR tuning band using front mirror bias currents up to 25 mA ( $5 \text{ kA/cm}^2$ ) with a back mirror current of 5 mA ( $0.3 \text{ kA/cm}^2$ ). The lasers achieved threshold currents of  $\sim 35 \text{ mA}$ , fiber-coupled powers up to 10 dBm, and a side-mode suppression ratio (SMSR) of over 35 dB for wavelengths from 1542 to 1569 nm.

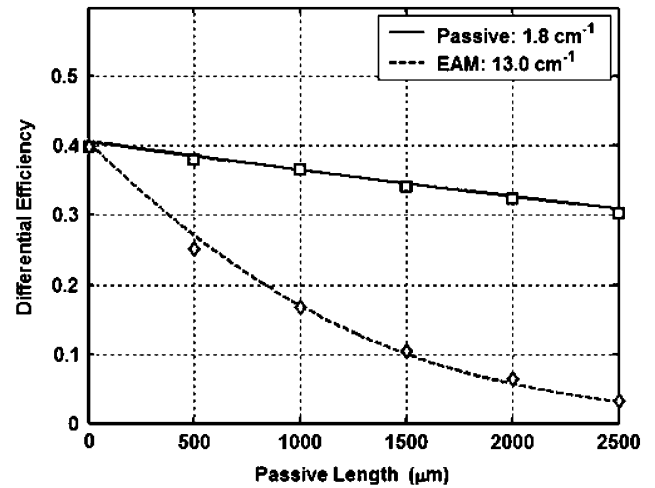


Fig. 9. Differential efficiency of active/passive lasers versus passive length used to extract modal propagation loss for passive and EAM regions at a wavelength of 1550 nm.

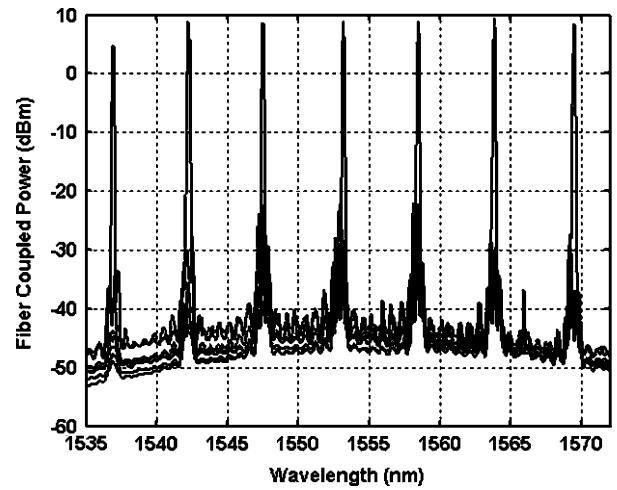


Fig. 10. Superimposed output spectrums tuned to different lasing wavelengths from SG-DBR laser with high gain output SOA.

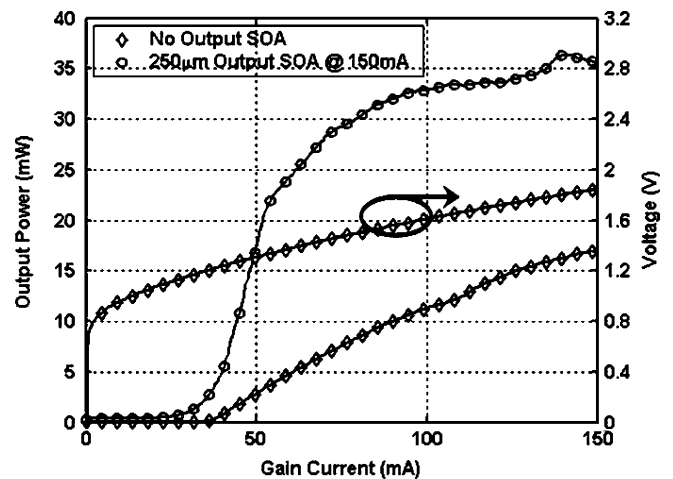
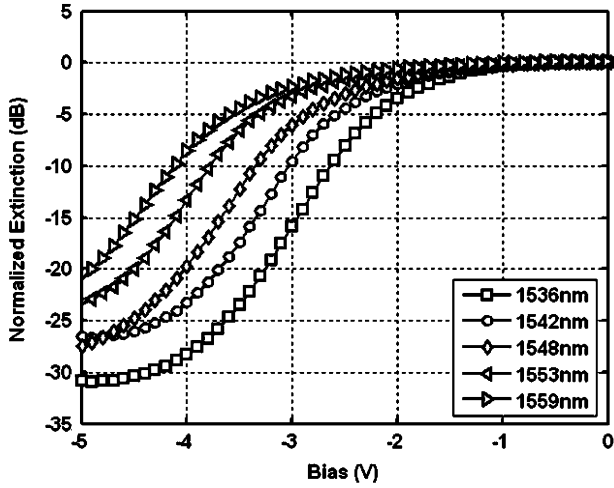


Fig. 11. Output power of SG-DBR laser captured in an integrating sphere for the case with no output SOA and with a 250- $\mu\text{m}$ -long SOA. The gain section voltage is indicated with the right-hand y-axis.

Fig. 12. Broadband DC extinction of a 125- $\mu\text{m}$ -long EAM.

The output power captured into an integrating sphere and voltage versus gain current (LIV) for SG-DBR lasers with no output SOA and for a device with a 250- $\mu\text{m}$ -long c-MQW SOA positioned after the front mirror are shown in Fig. 11. At a gain current of 150 mA, the device demonstrates over 16 mW of output power with no output SOA and over 35 mW of output power with an output SOA biased at 150 mA.

The broadband dc extinction characteristics from a 125- $\mu\text{m}$ -long EAM are shown in Fig. 12. The EAM provides 20–30 dB of total extinction with slope efficiencies of 14–16 dB/V for wavelengths from 1536 to 1560 nm. The 175- $\mu\text{m}$ -long EAMs provide 34–38 dB of total extinction with efficiencies over 20 dB/V. The efficient dc extinction properties are due to the combination of the high confinement factor provided by the c-MQW and the intermixing process that allows for precise placement of the modulator band-edge.

The small signal electrical to optical frequency response characteristics of 125- and 175- $\mu\text{m}$ -long EAMs were measured using a 50-GHz network analyzer and are shown in Fig. 13. The EAM electrodes were directly probed using ground-signal probes with a 50- $\Omega$  termination load. The stage temperature was again maintained at 18 °C. The optical 3-dB bandwidth was measured to be 39 GHz in the 125- $\mu\text{m}$ -long EAM and 32 GHz in the 175- $\mu\text{m}$ -long EAM.

Nonreturn to zero (NRZ) eye diagrams were taken at 40 Gb/s with a pseudorandom bit sequence (PRBS) of  $2^{31} - 1$  over the tuning range of a transmitter with a 125- $\mu\text{m}$ -long modulator. Fig. 14, presents the back-to-back input eye along with the output eyes from the device with a 1.5- $V_{\text{PtoP}}$  drive applied to the EAM. The eye diagrams are open and clear with extinction ratios (ER) over 8.7 dB for wavelengths up to 1560 nm at dc bias levels from 3.4 to 5.2 V. The average fiber-coupled output power under these conditions ranged from –5 to 0 dBm. The 1.5- $V_{\text{PtoP}}$  drive required in these devices approach the state-of-the-art discrete EAMs reported in [29], which required 0.79  $V_{\text{PtoP}}$  to drive over 10-dB ER.

The large signal chirp of the EAMs was measured at 10 Gb/s for wavelengths from 1541 to 1564 nm using Agilent's time

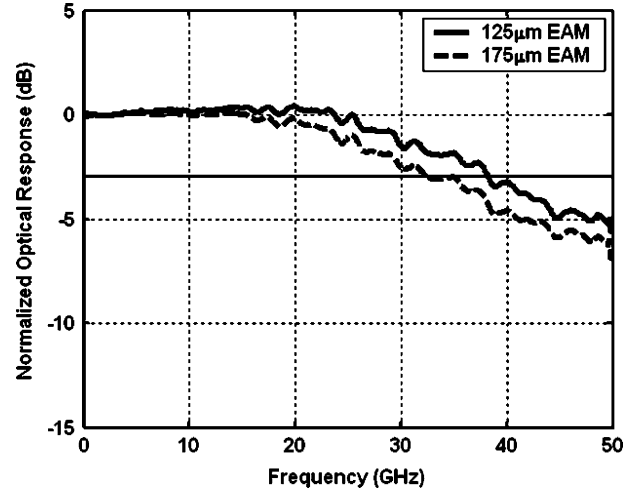
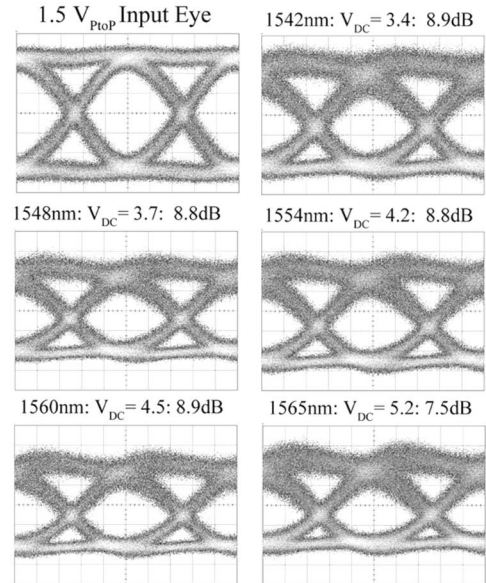
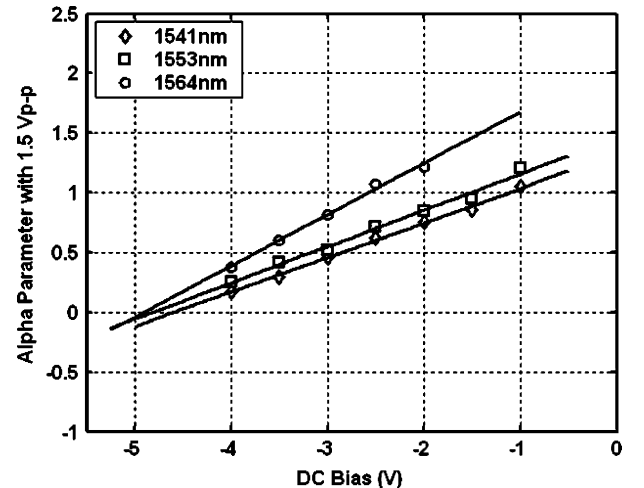


Fig. 13. Electrical-to-optical small signal response of EAMs.

Fig. 14. 40 Gb/s eye diagrams from 125- $\mu\text{m}$ -long EAM.Fig. 15. Large signal chirp parameter of EAM with a 1.5- $V_{\text{PtoP}}$  drive.

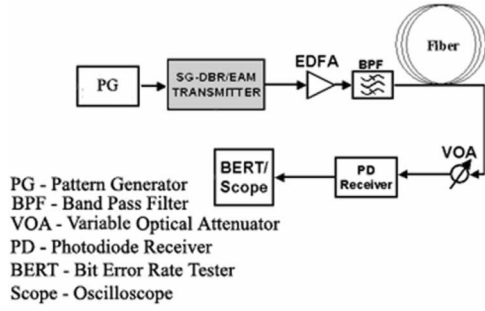


Fig. 16. Test set used for 40-Gb/s transmission measurements.

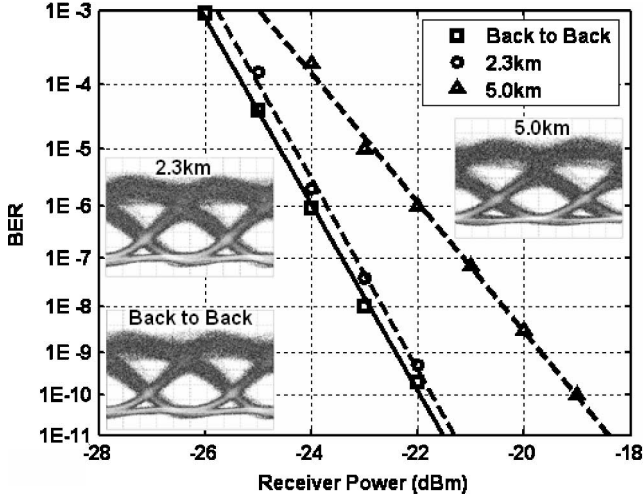


Fig. 17. BER measurements from 125- $\mu\text{m}$ -long EAM at 40 Gb/s with a 1.5- $V_{\text{PtoP}}$  drive and a wavelength of 1553 nm. The corresponding eye diagrams before and after transmission are shown as insets.

resolved chirp (TRC) software. The chirp parameter was measured as a function of the dc bias applied to the EAM with a 1.5- $V_{\text{PtoP}}$  drive applied to the device. As shown in Fig. 15, the chirp parameter is reduced with increasing reverse bias and decreasing wavelength. The measurement bias range was limited such that the lowest TRC measured chirp value was 0.15. However, the chirp parameter is expected to reach zero in the reverse bias range of 4.5–5.0 V.

Bit-error-rate (BER) measurements were made for 40-Gb/s transmission through 2.3 and 5 km of standard Corning SMF-28 fiber. A PRBS of  $2^7 - 1$  was used due to a noise floor resulting from a calibration issue in the BER tester (BERT) that manifested itself at longer word lengths. A schematic illustrating the BER test setup is shown in Fig. 16. In Fig. 17, the BER results and the respective eye diagrams are shown for a device employing a 125- $\mu\text{m}$ -long EAM at a wavelength of 1553 nm, a 1.5- $V_{\text{PtoP}}$  drive, and a dc bias of 4.9 V. As seen in the figure, the transmitter demonstrated only 0.2 dB of power penalty through 2.3 km and under 3 dB of penalty through 5.0 km. The BER was measured for a transmission through 2.3 km of fiber at wavelengths of 1542, 1553, and 1565 nm with the EAM biased in the 4.3–5.2-V range. Using the measured dispersion penalties of 0.4, 0.2, and 0.5 dB at the respective wavelengths and assuming a fiber dispersion of 16.45 ps/nm/km, the chirp parameters were calculated to be  $-0.15$ ,  $-0.25$ , and  $-0.1$ , re-

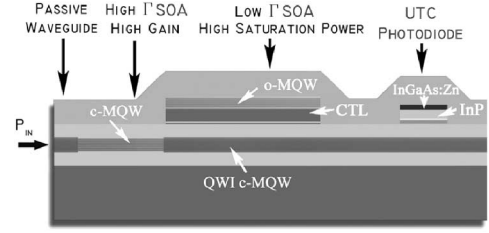


Fig. 18. Side-view schematic of receiver structure showing the high confinement c-MQW gain region (left), low-confinement o-MQW gain region (middle), and the UTC photodiode structure (right).

spectively. The lower chirp values than those shown in Fig. 15 are likely the result of the higher reverse biases used in the BER measurements.

The transmitter reported here is the first widely tunable EAM-based transmitter operating at 40 Gb/s. Previous EAM-based 40-Gb/s transmitter devices used single-frequency DFB lasers and typically relied on BJR [24]. The device reported in [24], demonstrated under 0.5-dB power penalty through 2.6 km of fiber at 1552 nm, required 2.5 $V_{\text{PtoP}}$  drive voltage, and provided 1.3 dBm of output power. Our transmitter offers lower drive voltage over a wide wavelength range and is integrated with a 40-Gb/s receiver.

### C. 40-Gb/s SOA/UTC Photodiode Receiver Performance

Waveguide receivers consisting of dual section SOAs and UTC photodiodes were placed on ridges parallel to the transmitters as depicted in the labeled SEM image of Fig. 4. Two different receiver designs were explored. The first made use of a 250- $\mu\text{m}$ -long high-gain c-MQW SOA section followed by a 1650- $\mu\text{m}$  high-saturation power o-MQW SOA section and a 30- $\mu\text{m}$ -long UTC photodiode. The second design made use of a 400- $\mu\text{m}$  long high-gain c-MQW SOA section followed by a 1500- $\mu\text{m}$  high-saturation power o-MQW SOA section and a 40- $\mu\text{m}$ -long UTC photodiode. A side-view schematic illustrating the receiver architecture is given in Fig. 18.

The continuous-wave (CW) gain properties of the dual section SOAs were characterized at an input wavelength of 1550 nm and are presented in Fig. 19 with the operation currents listed in the caption. The CW light was fed through a polarization controller and coupled into the input waveguide using a conical-shaped lensed fiber. The compressively strained QWs in the SOAs result in polarization sensitive performance. For maximum gain, the polarization controllers were used to couple only the transverse electric (TE) polarization mode into the device. Since the offset MQW used in the SOAs is independent of the laser gain region and is realized during regrowth, the SOA MQW could be redesigned for a polarization insensitive receiver.

As shown in Fig. 19, the design making use of a 250- $\mu\text{m}$ -long c-MQW section provides a peak gain of  $\sim 23$  dB and a saturation power of 18.6 dBm while the design using a 400- $\mu\text{m}$ -long c-MQW section provides a peak gain of  $\sim 28$  dB and a saturation output power of 18.2 dBm. These devices demonstrated only  $\sim 0.5$ -dB gain rolloff for wavelengths ranging from 1535 to 1565 nm. For increased saturation power, the CTL thickness



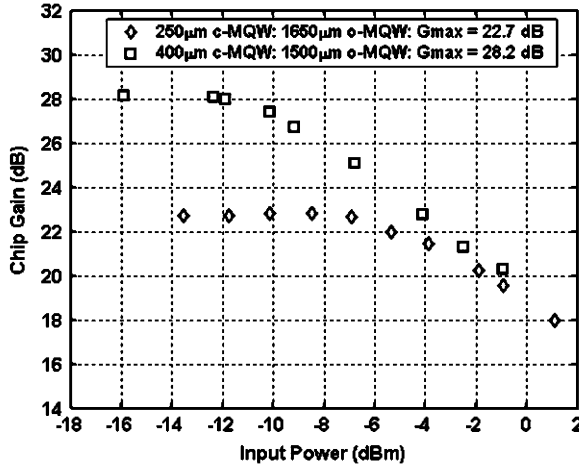


Fig. 19. Gain versus input power for dual section SOAs employing two different designs depicted in legend. In both cases the c-MQWs sections are operating at  $15 \text{ kA/cm}^2$  and the o-MQWs sections are operating at  $6 \text{ kA/cm}^2$  and the input wavelength is  $1550 \text{ nm}$ .

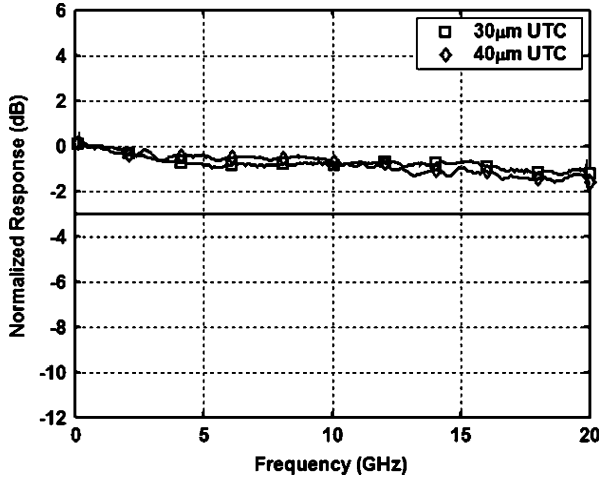


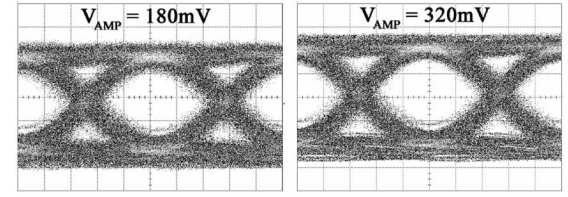
Fig. 20. Small signal response of 30- and 40- $\mu\text{m}$  UTC photodiodes with  $20 \text{ mA}$  of average photocurrent, a  $3\text{-V}$  reverse bias, and a  $25\text{-}\Omega$  termination.

could be increased as we have demonstrated  $19.5\text{--}20.2\text{-dBm}$  saturation output power with slightly different SOA designs [30].

The frequency response of the 30- and 40- $\mu\text{m}$ -long UTC photodiodes was measured using a 20-GHz Agilent lightwave component analyzer (LCA). A  $50\text{-}\Omega$  load was used on the RF probes for impedance matching within the RF cables. The result of this matching load is an effective termination load of  $25 \text{ }\Omega$  on the photodiode. Fig. 20 presents the response of the detectors with a  $3\text{-V}$  reverse bias and an average photocurrent level of  $20 \text{ mA}$ . As can be seen in the figure, the photodetectors demonstrate only  $1\text{--}1.5 \text{ dB}$  of rolloff at  $20 \text{ GHz}$ .

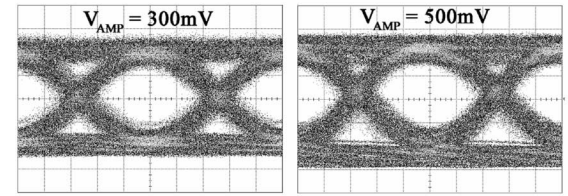
The internal quantum efficiency of the UTC photodiodes was measured to be between  $30\%\text{--}35\%$ . An error in the absorption coefficient used in the design simulations led to the choice of a nonoptimal absorber thickness. By increasing the thickness from  $50$  to  $100 \text{ nm}$  or above, the optical confinement in the

250 $\mu\text{m}$  c-MQW/1650 $\mu\text{m}$  o-MQW SOA: 30 $\mu\text{m}$  UTC



(a)

400 $\mu\text{m}$  c-MQW/1500 $\mu\text{m}$  o-MQW SOA: 40 $\mu\text{m}$  UTC



(b)

Fig. 21. 40 Gb/s eye diagrams. (a) Receiver design 1 at a c-MQW current density of  $12 \text{ kA/cm}^2$ . (b) Receiver design 2 at a c-MQW current density of  $8 \text{ kA/cm}^2$ . In both cases, the o-MQW sections were operated at  $5 \text{ kA/cm}^2$  and the detectors were biased at  $3 \text{ V}$ .

absorber would be increased such that the quantum efficiencies would reach the  $80\%\text{--}90\%$  range.

To demonstrate high-speed receiver functionality, eye diagrams and BER measurements were taken from the two different receiver designs at  $40 \text{ Gb/s}$ . A PRBS of  $2^7 - 1$  was used due to the noise floor in the BERT at longer word lengths. A  $40\text{-Gb/s}$  NRZ signal was fed through a band-pass filter, optical attenuator, and polarization controller before entering the input waveguide where it was then amplified in the SOA and detected in the UTC photodiode. Again the input signal was set to the TE polarization state for optimum performance. The output signal from the UTC passed through a bias tee that was connected directly to the oscilloscope or BERT. The optimal bias points of the receiver employing a  $250\text{-}\mu\text{m}$ -long c-MQW gain section followed by a  $1650\text{-}\mu\text{m}$  o-MQW gain section and a  $30\text{-}\mu\text{m}$ -long UTC photodiode were found to be  $12 \text{ kA/cm}^2$  in the c-MQW SOA section,  $5 \text{ kA/cm}^2$  in the o-MQW SOA section, and a reverse bias of  $3.3 \text{ V}$  on the detector. The receiver output eye diagrams presented in Fig. 21(a) are clear and open demonstrating up to a  $320\text{-mV}$  amplitude. If the sensitivity is defined as the power to achieve a BER of  $1\text{E-}9$ , the same receiver demonstrated a chip-coupled sensitivity of  $-16.8 \text{ dBm}$ , as shown in the  $40\text{-Gb/s}$  BER results of Fig. 22.

The optimal bias points for the receiver using a  $400\text{-}\mu\text{m}$ -long c-MQW gain section followed by a  $1500\text{-}\mu\text{m}$  o-MQW gain section and a  $40\text{-}\mu\text{m}$ -long UTC photodiode were found to be  $8 \text{ kA/cm}^2$  in the c-MQW SOA section,  $5 \text{ kA/cm}^2$  in the o-MQW SOA section, and a reverse bias of  $3.0 \text{ V}$  on the detector. The lower optimal current density on the longer c-MQW section of this SOA design was a result of the increasing amplified spontaneous emission (ASE) with current density. The receiver output eye diagrams presented in Fig. 21(b) are clear and open demonstrating up to  $500\text{-mV}$  amplitude over the  $25\text{-}\Omega$  termination. The chip-coupled sensitivity of this receiver design was  $-20.2 \text{ dBm}$ , as shown in Fig. 22. The improved sensitivity of

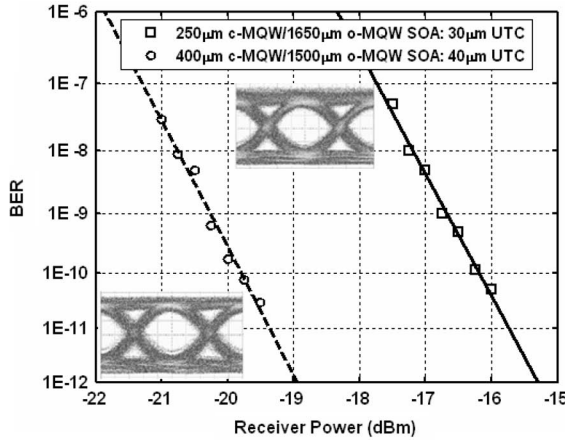


Fig. 22. 40 Gb/s BER versus received power for the two dual section SOA/UTC photodiode receiver designs with inset eye diagrams. The SOA operating conditions are identical to those stated in Fig. 21.

this receiver is due to the increased gain and quantum efficiency of the longer c-MQW SOA and photodetector, respectively.

State-of-the-art SOA preamplified receivers were reported in [25]. These impressive devices demonstrated a 40-Gb/s sensitivity of  $-17$  dBm, a maximum output amplitude of 250 mV, and required BJR. If an estimated 4-dB coupling loss is subtracted from the chip-coupled sensitivity for the receivers reported here, we arrive at a sensitivity of  $-16.2$  dBm, only slightly lower than that in [25]. However, the devices reported here can provide a  $2\times$  greater output amplitude of 500 mV and are integrated with widely tunable 40-Gb/s transmitters. With an expected 4–5-dB increase in the UTC photodiode quantum efficiency by using a 100-nm absorber, the sensitivity will be significantly improved.

#### D. 40-Gb/s Wavelength Conversion

With the ability to transmit and receive data at 40 Gb/s, the single-chip transceivers were tested as wavelength converters. A 40-Gb/s NRZ input signal with a PRBS of  $2^7 - 1$  was coupled into the SOA/UTC receiver for amplification and photodetection. The generated photocurrent was extracted from the UTC with a  $50\text{-}\Omega$  terminated probe, and then fed through a bias tee, a 26-dB gain RF amplifier, a 6- or 10-dB electrical attenuator, a second bias tee, and into the EAM using a  $50\text{-}\Omega$  probe. The EAM modulated the output wavelength from the widely tunable SG-DBR laser, resulting in wavelength conversion. The output optical signal was then fed through a variable optical attenuator and into a preamplified receiver before entering the BERT or oscilloscope. The complete test setup is shown in Fig. 23.

Back-to-back and wavelength converted 40-Gb/s eye diagrams are shown in Fig. 24 for a device making use of the dual section SOA design with a  $400\text{-}\mu\text{m}$ -long c-MQW section followed by a  $1500\text{-}\mu\text{m}$ -long o-MQW section and a  $40\text{-}\mu\text{m}$ -long photodiode in the receiver, and a  $175\text{-}\mu\text{m}$ -long EAM in the transmitter. The wavelength converted extinction ratios ranged from 10.6 to 11.8 dB for conversion from 1552 to 1542, 1553, and 1564 nm.

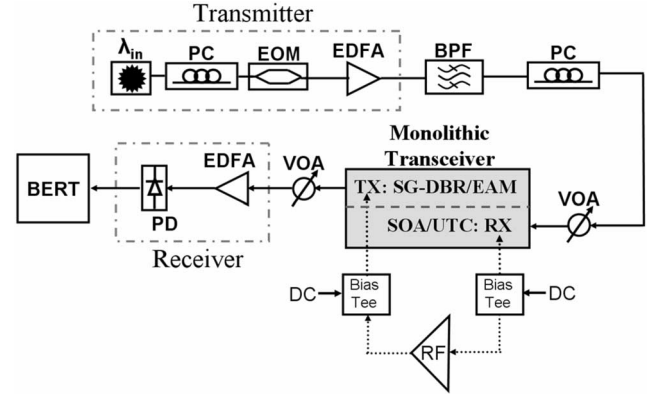


Fig. 23. Test setup used for 40-Gb/s wavelength converter testing. Schematic illustrates the monolithic transceiver from which the detected signal in the receiver is fed off-chip through an amplifier and then back into the EAM.

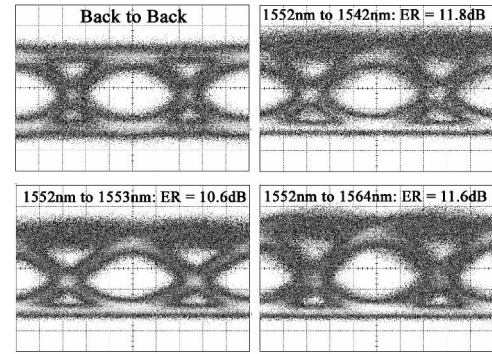


Fig. 24. 40-Gb/s back-to-back and wavelength converted eye diagrams from 1552 to 1542, 1553, and 1564 nm.

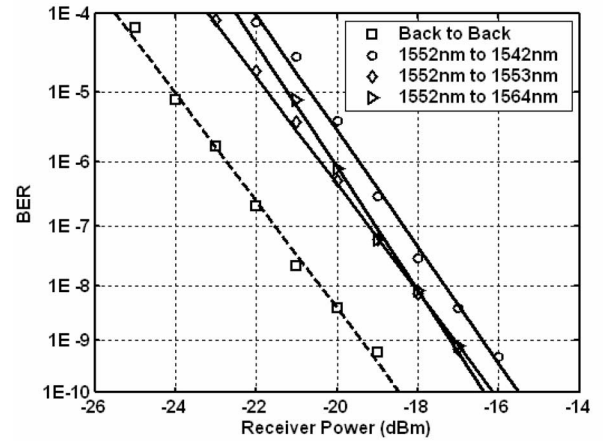


Fig. 25. 40-Gb/s wavelength conversion BER measurements from a transceiver device.

The back-to-back and wavelength converted BER measurements for the same device are shown in Fig. 25. As shown in the figure, error-free 40-Gb/s wavelength conversion is achieved. The device demonstrates between 2–3 dB of power penalty for conversion from 1552 nm to wavelengths of 1542–1564 nm. The optimal bias points for the wavelength conversion experiments were as follows: 1) chip-coupled input powers of  $-3$  to  $1$  dBm; 2) the  $400\text{-}\mu\text{m}$ -long high-gain

c-MQW section biased at 10 kA/cm<sup>2</sup>; 3) the 1500- $\mu$ m-long high-saturation power o-MQW section biased at 5 kA/cm<sup>2</sup>; 4) the 500- $\mu$ m-long laser gain section biased at 6–7 kA/cm<sup>2</sup>; 5) the output SOA biased at 1–2 kA/cm<sup>2</sup>; 6) the EAM reverse biased between 3–4.5 V; and 7) the photodiode reverse biased at 3–4 V. These operating conditions resulted in a fiber-coupled output power of between –0.5 and 0.5 dBm. Assuming a 4 dB per facet coupling loss, the device provided 3–7 dB of optical chip gain. The low optimal current density applied to the output SOA was a result of increased noise with increased bias level.

With an estimated electrical loss of 4–5 dB in the two bias tees and two RF cables, the total off-chip electrical gain is estimated to be 15–16 dB when a 6-dB attenuator was used and 11–12 dB when a 10-dB attenuator was used. This gain is in the vicinity of the loss associated with the low quantum efficiency of the UTC photodiodes since a 30%–35% internal quantum efficiency yields 9–10 dB of electrical loss over the case of 100% internal quantum efficiency. By modifying the UTC layer structure design the off-chip amplifier can be eliminated.

## VII. CONCLUSION

We demonstrate the first single-chip 40-Gb/s transceivers. The devices integrate SG-DBR lasers, QW-EAMs, low-confinement SOAs, and UTC photodiodes. These unique component structures represent extremely advanced technologies for their respective functions. A high-flexibility integration platform combining QWI and MOCVD regrowth was used for device fabrication. The relatively simple method relies on blanket MOCVD regrowth to avoid regrowth interfaces in the core of the optical waveguide and the use of a dielectric mask pattern on the growth surface.

The SG-DBR lasers demonstrate a tuning range of over 30 nm and an output power of 35 mW. The EAMs provided up to 39-GHz optical bandwidth and required only a 1.5-V<sub>PtoP</sub> drive to achieve nearly 9 dB of extinction. The low-drive-voltage widely tunable 40-Gb/s SG-DBR/EAM transmitters exhibit performance competitive with discrete single-frequency EAM based devices requiring BJR. The receiver SOAs achieved 23–28 dB of gain and saturation output powers up to 18.6 dBm, while the UTC photodiodes demonstrated 40-Gb/s operation. The –20.2-dBm chip-coupled SOA/UTC receiver sensitivity rivals state-of-the-art preamplified receivers requiring BJR. By using an off-chip electrical amplifier, we demonstrate low-power-penalty 40-Gb/s wavelength conversion.

## REFERENCES

- [1] T. L. Koch and U. K. Koren, "Semiconductor photonic integrated circuits," *IEEE J. Quantum Electron.*, vol. 27, no. 3, pp. 641–653, Mar. 1991.
- [2] M. Suzuki, Y. Noda, H. Tanaka, S. Akiba, Y. Kushihiro, and H. Ishiki, "Monolithic integration of InGaAsP/InP distributed feedback laser and electroabsorption modulator by vapor phase epitaxy," *J. Lightw. Technol.*, vol. LT-5, no. 9, pp. 1277–1285, Sep. 1987.
- [3] T. L. Koch, U. Koren, R. P. Gnall, F. S. Choa, F. Hernandez Gil, C. A. Burrus, M. G. Young, M. Oron, and B. I. Miller, "GaInAs/GaInAsP multiple quantum well integrated heterodyne receiver," *Electron. Lett.*, vol. 25, no. 24, pp. 1621–1623, 23, Nov. 1989.
- [4] R. J. Deri, T. Sanada, N. Yasuoka, M. Makiuchi, A. Kurumata, H. Hamaguchi, O. Wada, and S. Yamakoshi, "Low-loss monolithic integration of balanced twin-photodetectors with a 3 dB waveguide coupler for coherent lightwave receivers," *IEEE Photon. Technol. Lett.*, vol. 2, no. 8, pp. 581–584, Aug. 1990.
- [5] R. Nagarajan, C. H. Joyner, R. P. Schneider Jr., J. S. Bostak, T. Butrie, A. G. Dentai, V. G. Dominic, P. W. Evans, M. Kato, M. Kauffman, D. J. H. Lambert, S. K. Mathis, A. Mathur, R. H. Miles, M. L. Mitchell, M. J. Missey, S. Murthy, A. C. Nilsson, F. H. Peters, S. C. Pennypacker, J. L. Pleumeekers, R. A. Salvatore, R. K. Schlenker, R. B. Taylor, T. Huan Shang, M. F. Van Leeuwen, J. Webjorn, M. Ziari, D. Perkins, J. Singh, S. G. Grubb, M. S. Reffle, D. G. Mehuys, F. A. Kish, and D. F. Welch, "Large-scale photonic integrated circuits," *IEEE J. Sel. Topics Quantum Electron.*, vol. 11, no. 1, pp. 50–65, Jan./Feb. 2005.
- [6] E. J. Skogen, J. S. Barton, S. P. DenBaars, and L. A. Coldren, "A quantum-well-intermixing process for wavelength-agile photonic integrated circuits," *IEEE J. Sel. Topics Quantum Electron.*, vol. 8, no. 4, pp. 863–869, Jul./Aug. 2002.
- [7] M. K. Chin, "Comparative analysis of the performance limits of Franz-Keldysh effect and quantum confined Stark effect electroabsorption waveguide modulators," *Proc. Inst. Electr. Eng. Optoelectron.*, vol. 142, no. 2, pp. 109–114, Apr. 1995.
- [8] K. Morito, S. Tanaka, S. Tomabechi, and A. Kurumata, "A broadband MQW semiconductor optical amplifier with high saturation output power and low noise figure," presented at the Semiconductor Optical Amplifiers and their Applications Meeting, San Francisco, CA, 30 Jun. 2004, (PD1-1).
- [9] T. Ishibashi, T. Furuta, H. Fushimi, S. Kodama, H. Ito, T. Nagatsuma, N. Shimizu, and Y. Miyamoto, "InP/InGaAs uni-traveling-carrier photodiodes," *IEICE Trans. Electron.*, vol. E83-C, no. 6, Jun. 2000.
- [10] J. Binsma, P. Thijs, T. VanDongen, E. Jansen, A. Staring, G. VanDenHoven, and L. Tiemeijer, "Characterization of butt-joint InGaAsP waveguides and their application to 1310 nm DBR-type MQW gain-clamped semiconductor optical amplifiers," *IEICE Trans. Electron.*, vol. E80-C, pp. 675–681, 1997.
- [11] J. Wallin, G. Landgren, K. Streubel, S. Nilsson, and M. Öberg, "Selective area regrowth of butt-joint coupled waveguides in multi-section DBR lasers," *J. Cryst. Growth*, vol. 124, pp. 741–746, 1992.
- [12] M. Aoki, M. Suzuki, H. Sano, T. Kawano, T. Ido, T. Taniwatari, K. Uomi, and A. Takai, "InGaAs/InGaAsP MQW electroabsorption modulator integrated with a DFB laser fabricated by band-gap energy control selective area MOCVD," *IEEE J. Quantum Electron.*, vol. 29, no. 6, pp. 2088–2096, Jun. 1993.
- [13] M. N. Sysak, J. S. Barton, L. A. Johansson, J. W. Raring, E. J. Skogen, M. L. Mašanović, D. J. Blumenthal, and L. A. Coldren, "Single chip wavelength conversion using a photocurrent driven (PD) EA modulator integrated with a widely tunable sampled grating DBR (SGDBR) laser," *IEEE Photon. Technol. Lett.*, vol. 16, no. 9, pp. 2093–2095, Sep. 2004.
- [14] M. N. Sysak, J. W. Raring, J. S. Barton, M. Dummer, D. J. Blumenthal, and L. A. Coldren, "A single regrowth integration platform for photonic circuits incorporating tunable SGDBR lasers and quantum well EAMs," *IEEE Photon. Technol. Lett.*, vol. 18, no. 15, pp. 1630–1632, Aug. 2006.
- [15] M. M. Dummer, M. N. Sysak, J. W. Raring, A. Tauke Pedretti, L. A. Coldren, M. N. Sysak, J. W. Raring, D. J. Blumenthal, and L. A. Coldren, "Widely tunable single-chip transceiver for 10 Gb/s wavelength conversion," presented at the Device Research Conf., University Park, PA, Jun. 2006.
- [16] V. M. Menon, F. Xia, and S. Forrest, "Photonic integration using asymmetric twin-waveguide (ATG) technology: Part I—Concepts and theory," *IEEE J. Sel. Topics Quantum Electron.*, vol. 11, no. 1, pp. 17–29, Jan./Feb. 2005.
- [17] V. M. Menon, F. Xia, and S. Forrest, "Photonic integration using asymmetric twin-waveguide (ATG) technology: Part II—Devices," *IEEE J. Sel. Topics Quantum Electron.*, vol. 11, no. 1, pp. 30–42, Jan./Feb. 2005.
- [18] D. Deppe and N. Holonyak Jr., "Atom diffusion and impurity-induced layer disordering in quantum well III–V semiconductor heterostructures," *J. Appl. Phys.*, vol. 64, pp. 93–113, 1988.
- [19] S. K. Si, D. H. Yeo, K. H. Yoon, and S. J. Kim, "Area selectivity of InGaAsP-InP multiquantum-well intermixing by impurity-free vacancy diffusion," *IEEE J. Sel. Topics Quantum Electron.*, vol. 4, no. 8, pp. 619–623, Jul./Aug. 1998.
- [20] B. C. Qui, A. C. Bryce, R. M. de la Rue, and J. H. Marsh, "Monolithic integration in InGaAs-InGaAsP multiquantum-well structure using laser processing," *IEEE Photon. Technol. Lett.*, vol. 10, no. 6, pp. 769–771, Jun. 1998.
- [21] S. Charbonneau, P. Poole, Y. Feng, G. Aers, M. Dion, M. Davies, R. Goldberg, and I. Mitchell, "Band-gap tuning of InGaAs/InGaAsP/InP laser using high energy ion implantation," *Appl. Phys. Lett.*, vol. 67, pp. 2954–2956, 1995.

- [22] E. J. Skogen, J. W. Raring, J. S. Barton, S. P. DenBaars, and L. A. Coldren, "Post-growth control of the quantum-well band-edge for the monolithic integration of widely tunable lasers and electroabsorption modulators," *IEEE J. Sel. Topics Quantum Electron.*, vol. 9, no. 5, pp. 1183–1190, Sep./Oct. 2003.
- [23] E. Skogen, J. Raring, G. Morrison, C. Wang, V. Lal, M. Masonovic, and L. Coldren, "Monolithically integrated active components: A quantum well intermixing approach," *IEEE J. Sel. Topics Quantum Electron.*, vol. 11, no. 2, pp. 343–355, Mar./Apr. 2005.
- [24] M. Okayasu, M. Akashi, and M. Aoki, "A 1550-nm 40-Gb/s electroabsorption DFB laser diode module for transponders with very short reach (< 2 km) applications," in *Proc. IEEE LEOS Annu. Meeting Conf.*, Puerto Rico, Nov. 7–11, 2004, vol. 2, pp. 513–515.
- [25] B. Mason, J. M. Geary, J. M. Freund, A. Ougazzaden, C. Lentz, K. Glogovsky, G. Przybylek, L. Peticolas, F. Walters, L. Reynolds, J. Boardman, T. Kercher, M. Rader, D. Monroe, L. Ketelsen, S. Chandrasekhar, and L. L. Buhl, "40 Gb/s photonic integrated receiver with  $-17$  dBm sensitivity," in *Proc. Opt. Fiber Commun. Conf. Exhib.*, Mar. 17–22, 2002, pp. FB10-1–FB10-3.
- [26] V. Jayaraman, Z. Chuang, and L. Coldren, "Theory, design, and performance of extended tuning range semiconductor lasers with sampled gratings," *IEEE J. Quantum Electron.*, vol. 29, no. 6, pp. 1824–1834, Jun. 1993.
- [27] J. Raring, E. Skogen, S. DenBaars, and L. Coldren, "A study of regrowth interface and material quality for a novel InP based architecture," *J. Cryst. Growth*, vol. 273, no. 1–2, pp. 26–37, Dec. 2004.
- [28] J. W. Raring, E. J. Skogen, C. S. Wang, J. S. Barton, G. B. Morrison, S. Demiguel, S. P. DenBaars, and L. A. Coldren, "Design and demonstration of novel quantum well intermixing scheme for the integration of UTC-type photodiodes with QW-based components," *IEEE J. Quantum Electron.*, vol. 42, no. 2, pp. 171–181, Feb. 2006.
- [29] T. Yamanaka, K. Tsuzuki, N. Kikuchi, E. Yamada, Y. Shibata, H. Fukano, H. Nakajima, Y. Akage, and H. Yasaka, "High-performance InP-based optical modulators," in *Proc. IEEE/OEA Opt. Fiber Commun. Conf. and Nat. Fibre Opt. Eng. Conf.* Mar. 5–10, 2006.
- [30] J. Raring, E. Skogen, M. Mašanović, S. DenBaars, and L. Coldren, "Demonstration of high saturation power/high gain SOAs using quantum well intermixing and MOCVD regrowth," *Electron. Lett.*, vol. 41, no. 24, pp. 1345–1346, Nov. 2006.



**Larry A. Coldren** received the Ph.D. degree in electrical engineering from Stanford University, Stanford, CA in 1972.

After 13 years in the research area at Bell Laboratories, he joined the University of California, Santa Barbara (UCSB), in 1984, where he is now the Fred Kavli Professor of optoelectronics and sensors, and the Director of the Optoelectronics Technology Center. In 1990, he cofounded Optical Concepts, later acquired as Gore Photonics, to develop novel vertical-cavity surface-emitting laser (VCSEL) technology and in 1998 he cofounded Agility Communications to develop widely tunable integrated transmitters. At Bell Laboratories, he initially worked on waveguided surface-acoustic wave signal processing devices and coupled-resonator filters. He later developed tunable coupled-cavity lasers using novel reactive-ion etching (RIE) technology that he created for the then new InP-based materials. At UCSB he continued work on multiple-section tunable lasers, inventing, in 1988, the widely tunable multi-element mirror concept. During the late 1980s, he also developed efficient vertical-cavity multiple-quantum-well modulators, which led to novel VCSEL designs that provided unparalleled levels of performance. His current research interests include developing new photonic integrated circuit (PIC) and VCSEL technology, including the underlying materials growth and fabrication techniques, creation of vertical and in-plane GaN-based emitters, efficient all-epitaxial InP-based VCSELs, and a variety of PICs incorporating numerous optical elements for widely tunable integrated transmitters, receivers, and wavelength converters. He has authored or coauthored over 700 papers, five book chapters, one textbook, and is a holder of 36 patents.

Prof. Coldren has presented dozens of invited and plenary talks at major conferences. He is a Fellow of the Optical Society of America and Institute of Electrical Engineers, and a member of the National Academy of Engineering. He was the recipient of the 2004 John Tyndall Award.



**James W. Raring** was born in Ramsey, NJ, in 1978. He received the B.S. degree from California Polytechnic State University, San Luis Obispo, in 2001 and the Ph.D. degree in materials science from the University of California, Santa Barbara, in 2006.

His dissertation focuses on the design, growth, and fabrication of high-functionality wavelength-agile photonic integrated circuits operating at 10 and 40 Gb/s. The photonic circuits are based on sampled grating DBR lasers, electroabsorption modulators, semiconductor optical amplifiers, and photodiodes.

His work explores novel integration methods coupling quantum-well intermixing with straightforward MOCVD regrowth steps. He has authored or coauthored over 70 technical papers.

Dr. Raring is a member of the Optical Society of America and The International Society for Optical Engineering.